Article

High Resolution Crystal Structure of the Pyruvate Kinase Tetramer in Complex with the Allosteric Activator Mitapivat/AG-348

Xiao Han [1], Tatyana Sandalova [1], Cheng Zhang [2], Adil Mardinoglu [2,3], Adnane Achour [1,*] and Renhua Sun [1,*]

1   Science for Life Laboratory, Department of Medicine Solna, Karolinska Institute and Division of Infectious Diseases, Karolinska University Hospital, 17165 Stockholm, Sweden; xiao.han@ki.se (X.H.); tatyana.sandalova@ki.se (T.S.)
2   Department of Protein Science, Science for Life Laboratory, KTH-Royal Institute of Technology, 17121 Stockholm, Sweden; cheng.zhang@scilifelab.se (C.Z.); adilm@scilifelab.se (A.M.)
3   Centre for Host-Microbiome Interactions, Faculty of Dentistry, Oral & Craniofacial Sciences, King's College London, London SE1 9RT, UK
*   Correspondence: adnane.achour@ki.se (A.A.); renhua.sun@ki.se (R.S.)

Abstract: Pyruvate kinase (PK) deficiency is a rare genetic disorder that affects this critical enzyme within the glycolysis pathway. In recent years, Mitapivat (MTPV, AG-348) has emerged as a notable allosteric activator for treating PK deficiency. However, the allosteric regulatory effects exerted on PK by MTPV are yet to be comprehensively elucidated. To shed light on the molecular mechanisms of the allosteric effects, we employed crystallography and biophysical methods. Our efforts yielded a high-resolution crystal structure of the PK tetramer complexed with MTPV at 2.1 Å resolution. Isothermal titration calorimetry measurements revealed that MTPV binds to human PK with an affinity of 1 μM. The enhanced structural details now allow for unambiguous analysis of the MTPV-filled cavity intricately embedded within the enzyme. Finally, the structure suggests that MTPV binding induces an allosteric effect on the B-domain situated proximal to the active site. In summary, our study provides valuable insights into the allosteric regulation of PK by MTPV and paves the way for further structure-based drug optimization for therapeutic interventions in PK deficiency.

Keywords: human pyruvate kinase; PK deficiency; Mitapivat; crystal structure

1. Introduction

Pyruvate kinases (PK) play a pivotal role in cellular metabolism by catalyzing the transfer of the phosphate group from phosphoenolpyruvate (PEP) to adenosine diphosphate (ADP). This conversion results in the production of adenosine triphosphate (ATP) and pyruvic acid during the final stages of glycolysis [1]. The generation of pyruvate is essential for a multitude of critical energetic and biosynthetic pathways. The functional activity of PK enzymes is highly regulated by various allosteric effectors, which influence and coordinate conformational changes within specific regions of the protein structures [2]. Human PK enzymes are homotropically activated by PEP and heterotropically by monophosphorylated or biphosphorylated sugars [3]. In humans, four distinct tissue-specific PK isoforms exist: PKL, PKR, PKM1, and PKM2. Each isoform possesses kinetic properties tailored to accommodate the diverse metabolic requirements of different tissues. PKL and PKR predominate in the liver and red blood cells, respectively, while PKM1 is expressed in skeletal muscle and brain tissue, and PKM2 is primarily found in fetal tissue. Notably, the overexpression of PKM2 has garnered significant research attention in various cancer cell types [4,5].

A considerable number of crystal structures of PK molecules have been determined thus far, revealing a well-conserved three-dimensional architecture. In this structure, four

identical subunits form a tetramer. The domain organization of each monomeric subunit consists of a short N-terminal helical domain, followed by a (β/α) 8-barrel A-domain composed of two segments spanning residues 55–127 and 231–399. Additionally, there is a slightly irregular B-domain (also known as the lid domain) composed of residues 128–230, which is inserted between strand β3 and helix α3 of the A domain. Finally, the C-domain (residues 400–543) exhibits an α + β topology [2,6]. Residues originating from the C-domains contribute to the formation of a small interface within the PK tetramers, while a larger interface is constituted by residues from the A-domains. The active site of PK is situated between the A and B domains at the C-termini of the β-strands of the (β/α)$_8$ barrel (Supplementary Figure S1).

Fructose 1,6-bisphosphate (FBP), a glycolysis intermediate, is the most widely recognized and studied allosteric activator of human PK enzymes. It is anchored within the C-domain and positioned 40 Å away from the active site (Supplementary Figure S1). When FBP binds to PK, it activates the enzyme, facilitating the conversion of PEP to pyruvic acid and the production of ATP [2,6,7]. Both PKR and PKL tetramers exist in equilibrium between two distinct conformational states. The activated R-state, stabilized by PEP and FBP, is characterized by high substrate affinity and actively promotes the glycolytic pathway. In contrast, the inactivated T-state exhibits low substrate affinity. When PKs are bound and stabilized by ATP and alanine, this T-state leads to phosphorylation and the inhibition of glycolysis [8]. Additional comparative crystal structure analyses of mutated human PK variants revealed a conformational toggle between open and closed conformations of the allosteric loop following FBP binding [2,9,10].

Pyruvate kinase deficiency is a rare genetic disorder caused by mutations in the gene encoding PKLR, which impairs the glycolytic capacity of this pivotal enzyme [11–13]. More than 250 mutations in the PKLR gene have been identified and linked to PK deficiency. These genetic alterations disrupt the normal function of the enzyme, impairing its ability to catalyze the conversion of phosphoenolpyruvate (PEP) to pyruvate during glycolysis [14,15]. As a result, energy production within red blood cells is compromised, leading to a cascade of effects, including ATP depletion and structural modifications in the cell membrane, culminating in hemolysis [16,17]. This condition primarily presents as hemolytic anemia, characterized by the premature destruction of red blood cells, leading to a shortened lifespan of these cells in circulation [18]. Clinical management strategies for PK deficiency primarily focus on symptom relief and may include blood transfusions in severe cases. Hematopoietic stem cell transplantation has also been explored as a potential curative intervention [19]. Mitapivat (MTPV, also known as AG-348), has been identified as a small-molecule allosteric activator of PKL, demonstrating efficacy not only on the wild-type enzyme but also on the mutant forms associated with hemolytic anemia. MTPV, brand name Pyrukynd (Agios Pharmaceuticals, Cambridge, MA, USA), is approved for the treatment of hemolytic anemia in adults with PK deficiency in the USA, EU, and UK.

Although a crystal structure of the PK/MTPV complex has been previously reported, determined at a resolution of 2.7 Å [20,21], the structural data have not been deposited in the Protein Data Bank. As acknowledged [20], the quality and coverage of the electron density map did not permit an unambiguous description of MTPV in the formed complex. Moreover, despite the substantial amount of structural knowledge accumulated for PKs, the precise molecular foundations that underlie the allosteric regulatory effects remain to be fully elucidated for PKs. In this study, we present a higher resolution crystal structure of the PK tetramer in complex with MTPV, determined at a resolution of 2.1 Å. The significantly improved resolution of the three-dimensional structure of the formed complex facilitated a meticulous atomic analysis of the MTPV-occupied cavity, yielding valuable insights into the precise positioning and interactions formed between the allosteric activator and the PK enzyme. The structure analysis revealed that the shift in PK activity following MTPV binding could be attributed to the allosteric effects on the B-domain, adjacent to the active site.

2. Materials and Methods

2.1. Cloning, Expression, and Purification of the Isoform L-Type of Pyruvate Kinase

The codon-optimized DNA sequence encoding human PKLR isoform 2 (accession No. NP_870986) was synthesized. A Fast-Cloning method [22] was utilized to construct the codon-optimized DNA sequence, along with a cloning facilitation sequence outlined in Supplementary Table S1, into the expression vector pET-28a (Novagen, Madison, WI, USA). The integrity of the expression construct was verified through sequencing. The construct was then transformed into chemically competent *E. coli* BL21 Star (DE3) cells (Thermo Fisher, Waltham, MA, USA). A single colony of the transformed cells was inoculated and cultured overnight in TB medium supplemented with 50 μg/mL kanamycin. The culture was incubated in a 120 rpm orbital shaking incubator at 37 °C. Once the optical density at 600 nm reached 0.85, protein overexpression was initiated by adding 0.9 mM isopropyl β-D-1 thiogalactopyranoside (IPTG), followed by further cultivation for 4.5 h. Cells were harvested, and the cell pellet was stored at −20 °C. All purification steps were conducted at 4 °C, and the target protein purity was confirmed using SDS-PAGE for each purification step. An 18 g cell pellet was lysed in 160 mL buffer via ultrasonication. The lysis buffer comprised 10 mM HEPES, pH 7.5, 2 mM $MgCl_2$, 2 mM DTT, 10 mM KCl, and 1 mM PMSF. One-third of the supernatant obtained after centrifugation at $40,000 \times g$ for 40 min was subjected to anion exchange chromatography employing two series-connected HiTrap Q HP columns (GE Healthcare, Chicago, IL, USA). Elution was performed with a 0 to 30% increasing buffer B over 20 min at a flow rate of 2.5 mL/min. Buffer A consisted of 10 mM HEPES, pH 7.5, and 2 mM $MgCl_2$, while buffer B contained an additional 1 M NaCl. Fractions containing the pure target protein were pooled, concentrated to 1.5 mL in an ultra-centrifugal tube, and subsequently subjected to size exclusion chromatography (SEC) using a Superdex 200 Prep Grade (Cytiva, Marlborough, MA, USA) column. The running buffer for SEC was 10 mM HEPES, pH 7.5, and 150 mM NaCl. Fractions confirmed to contain the target protein (Supplementary Figure S2) were pooled, concentrated to 16.5 mg/mL, flash-frozen using liquid nitrogen, and stored in a −80 °C freezer.

2.2. Crystallization

Crystallization was performed using the sitting-drop vapor diffusion method at 293.15 K. A 60 μL aliquot of 16.5 mg/mL protein solution was mixed with 20 μL buffer C, comprising 10 mM HEPES, pH 7.5, 5.76 mM $MgCl_2$, 288 mM KCl, and 28.8 mM Fructose-1,6-Bisphosphate (FBP) (Sigma-Aldrich, Burlington, MA, USA). Additionally, 7.2 μL 20 mM MTPV solution in DMSO was diluted with 28 μL 10 mM HEPES, pH 7.5. The protein and MTPV solutions were combined to form the complex. Drops were set up using 0.6 μL of the complex solution and 0.3 μL of the reservoir solution (0.2 M Magnesium formate dihydrate, 20% *w/v* Polyethylene glycol 3350), equilibrated against 100 μL of the reservoir solution in a 96-well protein crystallization plate (Corning, Corning, NY, USA). The plate was incubated at 20 °C in the Rock Imager 1000 (Formulatrix, Bedford, MA, USA), and the wells were imaged by Rock Imager (Formulatrix). Crystals appeared after 72 h of incubation. Subsequently, the crystals were harvested using mounted CryoLoops (Hampton Research, Aliso Viejo, CA, USA), cryoprotected with a solution containing 20% ethylene glycol in the reservoir solution, flash-frozen in liquid nitrogen, and transported to the beamline for data collection.

2.3. Data Collection and Processing

Diffraction images were collected in the automatic beamline ID30 at the European Synchrotron Radiation Facility (ESRF) in Grenoble, France. Data were collected at 100 K for a full sweep of 360° with an oscillation of 0.2°, with 0.05 s exposure time. Diffraction data were processed using autoPROC 1.1.7 pipeline [23]. The data collection and processing statistics are summarized in Table 1.

Table 1. Data collection, processing, and structure refinement statistics. Values in parentheses are for the outer shell.

Data Collection	
Wavelength (Å)	0.9655
Temperature (K)	100
Detector	PILATUS 32M
Crystal-to-detector distance (mm)	121.69
Rotation range per image (°)	0.2
Total rotation range (°)	360
Exposure time per image (s)	0.05
Data processing	
Space group	$P1$
a, b, c (Å)	84.93, 86.96, 91.55
α, β, γ (°)	76.78, 66.87, 80.22
Mosaicity (°)	0.11
Resolution range (Å)	84.32–2.10 (2.14–2.10)
Total No. of reflections	240,432 (12,275)
No. of unique reflections	131,759 (6456)
Completeness (%)	96.6 (94.8)
Multiplicity	1.8 (1.9)
$\langle I/\sigma(I)\rangle$	7.4 (4.6)
R_{meas}	0.054 (0.102)
$CC_{1/2}$	0.965 (0.963)
Overall B factor from Wilson plot ($Å^2$)	12.94
Refinement	
Final R_{work}	0.2317 (0.2646)
Final R_{free}	0.2653 (0.3135)
r.m.s. deviations	
Bond lengths (Å)	0.008
Angles (°)	1.012
Ramachandran plot	
Favored (%)	97.85
Allowed (%)	1.95
Outliers (%)	0.2
Average B-factor	30.32
Macromolecules	30.54
Ligands	25.31
Solvent	27.21

2.4. Structure Solution and Refinement

The crystal structure of the PK/MTPV complex was determined by molecular replacement, utilizing Phaser-MR [24] in PHENIX, with the structure of the apo form of PK (PDB entry 4IP7) [7] employed as the search model. Subsequent refinement was conducted using PHENIX 1.20.1-4487. Manual model building was conducted using Coot 0.9.8.92 [25], and

the resulting model was further refined using PHENIX [26–28]. Restraint dictionaries for Fructose-1,6-Bisphosphate (FBP) and MTPV were generated using the Grade Web Server (https://grade.globalphasing.org/cgi-bin/grade2_server.cgi) (accessed on 25 November 2022). The refinement statistics are summarized in Table 1. The figures were generated using PyMOL 2.6.0a0. The final coordinates/structure factors were submitted to the PDB, with the accession code 8XFD. The 2D interaction diagram was generated using PoseEdit in Protein Plus Server (https://proteins.plus) (accessed in February 2024) [29].

3. Results and Discussion

3.1. Thermodynamic Parameters for Pyruvate Kinase-MTPV Interactions

The thermodynamic characteristics of PK-MTPV interactions were explored using Isothermal Titration Calorimetry (ITC) with the iTC200 MicroCal (GE Healthcare). A series of 16 injections, each delivering 2.5 μL of 1 mM MTPV, were sequentially introduced into 100 mM PK within the cell. The interval between injections was set at 150 s to allow the signal to return to the baseline (Figure 1). The data were fitted to a one-site binding model using MicroCal PEAQ-ITC software 1.41 [30], yielding a dissociation constant (KD) of 1.03 ± 0.24 μM and a stoichiometry (N) of 0.599 ± 0.009. The value of the stoichiometry (N) implies that, within the context of a one-site binding model, approximately half of the binding sites were occupied during the binding event, meaning that two MTPV molecules bound to one PK tetramer. This observation is consistent with the stoichiometry observed in our crystal structure, as discussed in Section 3.2. The enthalpy change (ΔH) associated with the binding was -2.79 ± 0.09 kcal/mol, and the free energy change (ΔG) was -8.50 cal/(mol·K). The statistics for the ITC assays are summarized in Table 2.
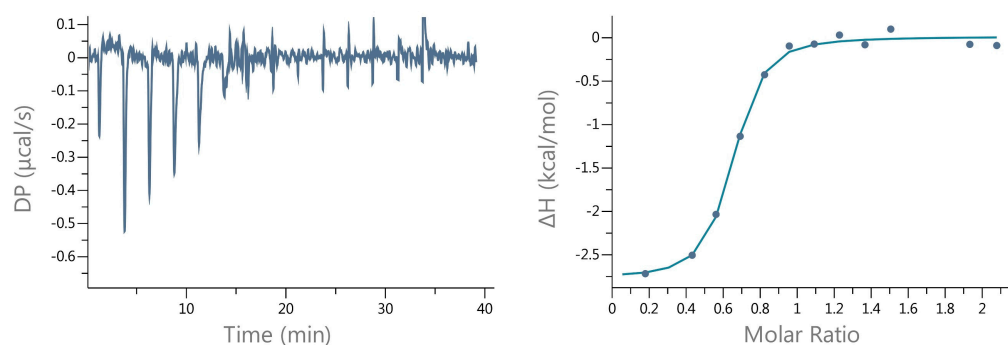

Figure 1. Isothermal titration calorimetry (ITC) assays reveal that MTPV exhibits a binding affinity of 1 μM towards pyruvate kinase.

Table 2. Statistics for isothermal titration calorimetry assay.

Normalized heat, ΔH (kcal/mol)	-2.79 ± 0.09
Baseline adjusted heat, offset (kcal/mol)	0.05 ± 0.03
Free energy change, ΔG (kcal/mol)	-8.50
Binding constant, KD (μM)	1.03 ± 0.24
Stoichiometry, N (sites)	0.599 ± 0.009

3.2. The Quality of the Electron Density Allows for the Unambiguous Positioning of MTPV

The PK tetramer is organized as a dimer of dimers. The ligand positioning was unequivocal, as evidenced by the 2Fo-Fc map (Figure 2). The identification process revealed the presence of two MTPV- and four FBP molecule-binding sites. Mg_{2+} ions were assigned to each active site, but they did not directly contribute to the binding of MTPV or FBP (Figure 2). The binding sites of the MTPVs were near the central region of the enzyme tetramer, in locations that were distinct from the FBP sites. MTPVs were strategically

positioned at the interfaces formed by the dimer subunits, establishing hydrogen bonds, π-stacking, and hydrophobic interactions with PK (Figure 3). The MTPV molecules occupied symmetrical pockets adjacent to the phenylalanine residues F36 from subunits C and D (or A and B) (Figures 2 and 3). Given that MTPV is not a symmetrical molecule, its binding is also asymmetrical. The quinoline moiety of MTPV partakes in hydrophobic interactions with the leucine residue L404 on subunit D (or B), while residue L404 on subunit C (or A) is proximate to the cyclopropylmethyl moiety on the opposite side of the pocket (Figure 3). However, these disparities do not induce noticeable conformational alterations of the two monomers surrounding the pocket. Superimposing monomer C onto D reveals that the side chain of residue F36 from subunit D undergoes a rotation of nearly 90 degrees, which results in a non-symmetrical binding site. The rotated side chain of F36 becomes orthogonal to the central phenalene ring of MTPV, thereby augmenting π-π interactions between them. Moreover, two water molecules in proximity to the quinoline moiety contribute to the formation of a hydrogen bond network between MTPV and the backbone/sidechain atoms of PK residues, N328, V362, R455, and R477 (Figure 3). Direct hydrogen bonds further amplify the binding interactions between PK and MTPV. One of the two oxygen atoms of the sulfonamide forms a hydrogen bond with the backbone nitrogen of the tyrosine residue Y400 in subunit D. The nitrogen adjacent to the sulfonamide also forms a hydrogen bond with the backbone oxygen of the leucine residue L363 on subunit D; the carbonyl oxygen from the other side of the phenalene ring interacts with the side chain of K321 from subunit C (Figure 3). Consequently, MTPV appears to function as a hairpin that efficiently connects two monomers within the PK tetramer (Figures 2 and 3).
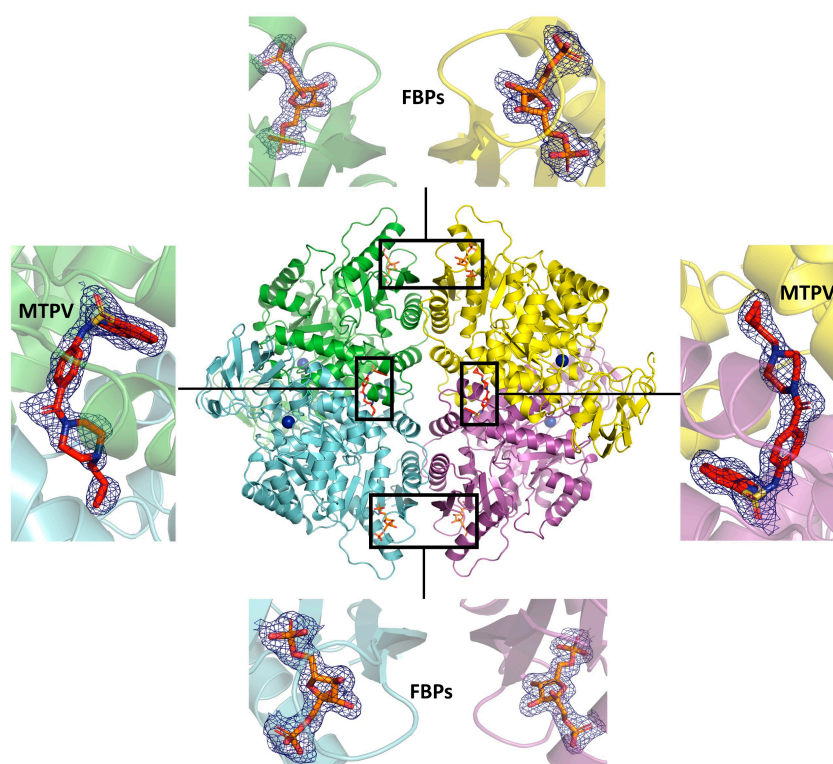

Figure 2. MTPV and FBP interact with the human pyruvate kinase at separate sites. The PK tetramer is composed of four monomeric subunits depicted in green, cyan, yellow and magentas, respectively. MTPV and FBP are represented as stick models, with carbon atoms colored in red or orange, nitrogen in blue, oxygen in red, and sulfur in yellow. The binding sites are enlarged to highlight the unambiguous electron densities of the ligands. The 2Fo-Fc maps, exhibited at 1σ and surrounding the ligands, are depicted as blue meshes. The Mg_{2+} ions bound in each active site are represented as blue spheres.
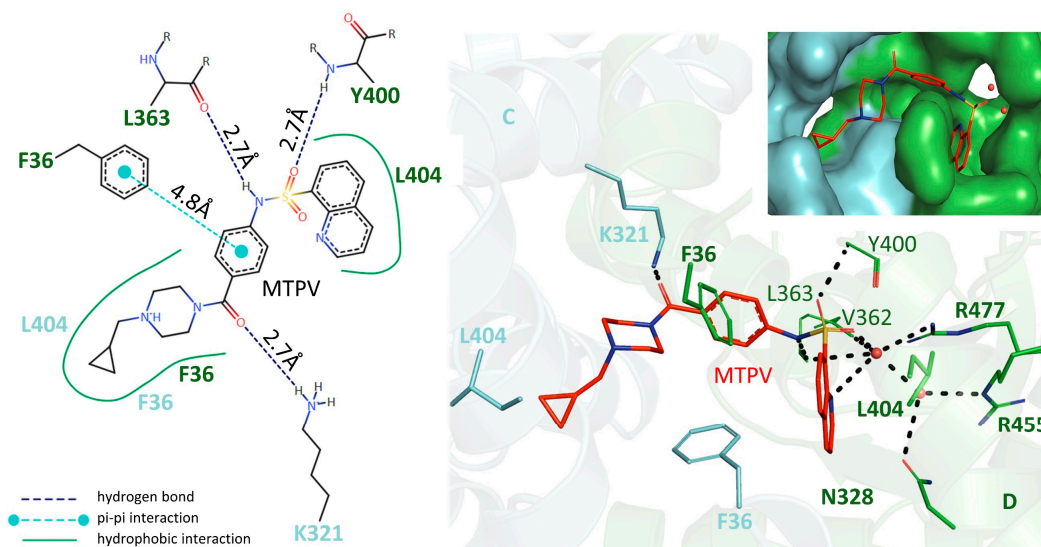
Figure 3. Interactions between pyruvate kinase and MTPV. The hydrogen bonds are depicted as blue dashed lines in a 2D interaction diagram (**left panel**). Hydrophobic contacts are indicated by green dashed lines. The π- π interaction is shown by pale-cyan dashed line. The lengths of the three direct hydrogen bonds and the distance of the formed π- π interactions are labeled. A zoomed-in view of the MTPV binding pocket (**right panel**) displays all residues from subunits C and D that interact with MTPV. The lengths of the water-mediated hydrogen bonds are 3.2 ± 0.3 Å. The side chains are represented as sticks and the main chains as lines. Water molecules are shown as red spheres, and hydrogen bonds are depicted as black dashed lines. An inset figure in the upper right corner illustrates a surface model of the MTPV binding cavity formed between subunits C and D. The adjacent subunits C and D are colored green and cyan, respectively. The coloring scheme of MTPV is the same as that in Figure 2.

3.3. The Binding of MTPV Potentially Triggers an Allosteric Effect on the B-Domain Situated Proximal to the Active Site

Upon superimposing the PK/FBP/citrate complex (PDB entry 4IP7) [7] onto our PK/FBP/MTPV structure, we did not observe significant shifts in the A- and C-domains. However, a rotation of approximately 12° was observed in the B-domain, which is situated distal to the MTPV binding site (Figure 4). Although this rotation may or may not be attributed to citrate binding in the active site, given that our structure does not include citrate, there remains the possibility that MTPV binding induces a long-range allosteric effect. In such a scenario, the subtle conformational alterations in the A- and C-domains may not be immediately discernible through crystallographic analysis. It is only when the impact of MTPV binding extends to the distal B-domain that the allosteric effect becomes pronounced. Concurrently, we sought to understand the packing mechanism of tetramers during crystallization, specifically how MTPVs maintain a consistent orientation—a prerequisite for the specific MTPV orientations solved within the present crystal structure. Our findings reveal that the binding of the asymmetrical MTPV molecule leads to shifts of the two B-domains within the same dimer, while this shift was not observed in the previously solved PK/FBP/citrate structure [7] (Supplementary Figure S3). This phenomenon accounts for the oriented stacking of the tetramers. Thus, the subtle differences between the two ends of the MPTV molecule can induce differences for the two distant B-domains within the same dimer. If this is indeed the case, it could provide compelling evidence that MTPV binding triggers allosteric effects on the B-domain.
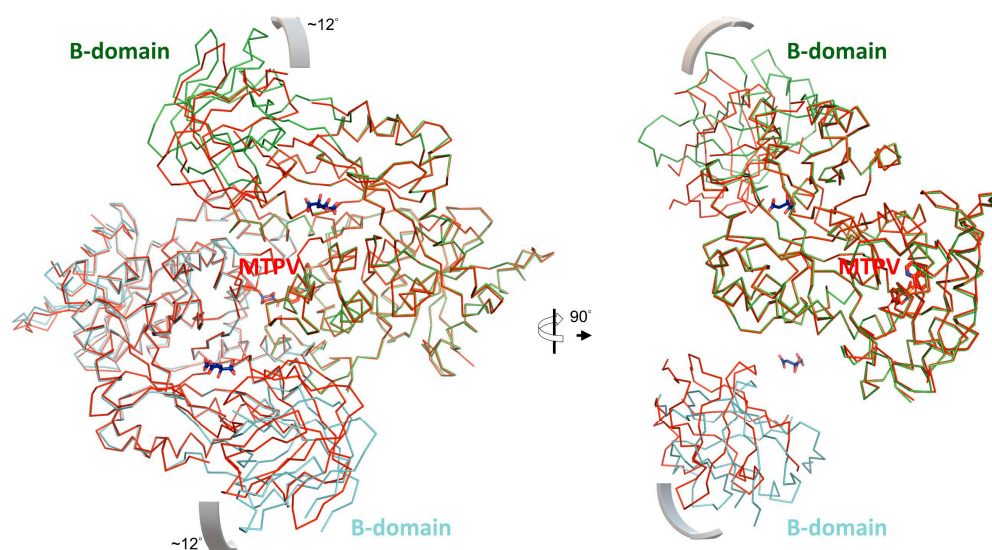
Figure 4. The B-domains undergo a rotational shift in the PK/MTPV complex compared to the PK/FBP/citrate complex. For clarity, only two monomeric subunits of the MTPV-bound PK tetramer are illustrated in green and cyan. The two PKs from the PK/FBP/citrate complex are shown in red, with citrates in the active sites. Proteins are shown as ribbons. MTPV and citrates are represented as stick models, with carbon atoms colored in red or blue, nitrogen in blue, oxygen in red, and sulfur in yellow. In the right panel, domains other than the B-domain within a single PK monomer are hidden for clarity.

Intriguingly, a distinct class of allosteric modulators has been recently identified to bind within the same pocket as MTPV [31]. Examination of several compounds containing sulfone-catechol unveiled that these innovative modulators can both stimulate and inhibit PK without inducing substantial conformational changes in the PK tetramer core. However, these compounds were soaked into pre-formed crystals of the apo form of a PK truncate, which lacked the B-domain entirely. Consequently, we suggest that the shift in PK activity following MTPV binding could be attributed to allosteric effects on the B-domain adjacent to the active site. Moreover, the formation of additional interactions between monomers via MTPV leads to dimer rigidification within each tetramer, resulting in a higher stabilization of the tetramer, which could also be a significant non-excluding factor underlying the enhanced function of mutated PK variants following treatment with MTPV.

In conclusion, our study provides an enhanced understanding of the allosteric regulation of PK by MTPV. The high-resolution structure of the PK/MTPV complex reveals the intricate interplay between MTPV and the enzyme, highlighting the potential allosteric effects on the B-domain, which in turn, remodels the active site. This finding is particularly significant as it suggests a novel mechanism of action for MTPV and possibly other allosteric modulators. These insights not only provide more comprehensive insights into the binding site of MTPV in human PK but also pave the way for the development of more effective therapeutic interventions. Future research could concentrate on investigating the effect of modified MTPV, leading to the discovery of new drugs with improved efficacy and safety profiles. The high-resolution structure of the complex can expedite structure-based drug optimization for therapeutic interventions in PK deficiency.

Supplementary Materials: The following supporting information can be downloaded at: https://www.mdpi.com/article/10.3390/cryst14050441/s1, Table S1; Figure S1: Crystallographic structure of the pyruvate kinase-MTPV complex; Figure S2: Size exclusion chromatography of the recombinant human pyruvate kinase; Figure S3: The binding of the MTPV molecule induces shifts in the two B-domains within the same dimer in the pyruvate kinase-MTPV complex, a phenomenon not observed in the PK/FBP/citrate complex; The appendix: Full wwPDB X-ray structure validation report.

References

1. Gupta, V.; Bamezai, R.N. Human pyruvate kinase M2: A multifunctional protein. *Protein Sci.* **2010**, *19*, 2031–2044. [CrossRef]
2. Schormann, N.; Hayden, K.L.; Lee, P.; Banerjee, S.; Chattopadhyay, D. An overview of structure, function, and regulation of pyruvate kinases. *Protein Sci.* **2019**, *28*, 1771–1784. [CrossRef]
3. Munoz, M.E.; Ponce, E. Pyruvate kinase: Current status of regulatory and functional properties. *Comp. Biochem. Physiol. Part B Biochem. Mol. Biol.* **2003**, *135*, 197–218. [CrossRef]
4. Li, Y.H.; Li, X.F.; Liu, J.T.; Wang, H.; Fan, L.L.; Li, J.; Sun, G.P. PKM2, a potential target for regulating cancer. *Gene* **2018**, *668*, 48–53. [CrossRef] [PubMed]
5. Christofk, H.R.; Vander Heiden, M.G.; Harris, M.H.; Ramanathan, A.; Gerszten, R.E.; Wei, R.; Fleming, M.D.; Schreiber, S.L.; Cantley, L.C. The M2 splice isoform of pyruvate kinase is important for cancer metabolism and tumour growth. *Nature* **2008**, *452*, 230–233. [CrossRef] [PubMed]
6. Valentini, G.; Chiarelli, L.R.; Fortin, R.; Dolzan, M.; Galizzi, A.; Abraham, D.J.; Wang, C.; Bianchi, P.; Zanella, A.; Mattevi, A. Structure and function of human erythrocyte pyruvate kinase. Molecular basis of nonspherocytic hemolytic anemia. *J. Biol. Chem.* **2002**, *277*, 23807–23814. [CrossRef] [PubMed]
7. Holyoak, T.; Zhang, B.; Deng, J.; Tang, Q.; Prasannan, C.B.; Fenton, A.W. Energetic coupling between an oxidizable cysteine and the phosphorylatable N-terminus of human liver pyruvate kinase. *Biochemistry* **2013**, *52*, 466–476. [CrossRef]
8. Morgan, H.P.; Zhong, W.; McNae, I.W.; Michels, P.A.; Fothergill-Gilmore, L.A.; Walkinshaw, M.D. Structures of pyruvate kinases display evolutionarily divergent allosteric strategies. *R. Soc. Open Sci.* **2014**, *1*, 140120. [CrossRef]
9. McFarlane, J.S.; Ronnebaum, T.A.; Meneely, K.M.; Chilton, A.; Fenton, A.W.; Lamb, A.L. Changes in the allosteric site of human liver pyruvate kinase upon activator binding include the breakage of an intersubunit cation-pi bond. *Acta Crystallogr. Sect. F Struct. Biol. Commun.* **2019**, *75*, 461–469. [CrossRef]
10. Ishwar, A.; Tang, Q.; Fenton, A.W. Distinguishing the interactions in the fructose 1,6-bisphosphate binding site of human liver pyruvate kinase that contribute to allostery. *Biochemistry* **2015**, *54*, 1516–1524. [CrossRef]
11. Fattizzo, B.; Cavallaro, F.; Marcello, A.; Vercellati, C.; Barcellini, W. Pyruvate Kinase Deficiency: Current Challenges and Future Prospects. *J. Blood Med.* **2022**, *13*, 461–471. [CrossRef] [PubMed]
12. Bianchi, P.; Fermo, E.; Lezon-Geyda, K.; van Beers, E.J.; Morton, H.D.; Barcellini, W.; Glader, B.; Chonat, S.; Ravindranath, Y.; Newburger, P.E.; et al. Genotype-phenotype correlation and molecular heterogeneity in pyruvate kinase deficiency. *Am. J. Hematol.* **2020**, *95*, 472–482. [CrossRef] [PubMed]
13. Bianchi, P.; Fermo, E. Molecular heterogeneity of pyruvate kinase deficiency. *Haematologica* **2020**, *105*, 2218–2228. [CrossRef] [PubMed]
14. van Wijk, R.; Huizinga, E.G.; van Wesel, A.C.; van Oirschot, B.A.; Hadders, M.A.; van Solinge, W.W. Fifteen novel mutations in PKLR associated with pyruvate kinase (PK) deficiency: Structural implications of amino acid substitutions in PK. *Hum. Mutat.* **2009**, *30*, 446–453. [CrossRef] [PubMed]
15. Zanella, A.; Fermo, E.; Bianchi, P.; Chiarelli, L.R.; Valentini, G. Pyruvate kinase deficiency: The genotype-phenotype association. *Blood Rev.* **2007**, *21*, 217–231. [CrossRef] [PubMed]
16. McMahon, T.J.; Darrow, C.C.; Hoehn, B.A.; Zhu, H. Generation and Export of Red Blood Cell ATP in Health and Disease. *Front. Physiol.* **2021**, *12*, 754638. [CrossRef] [PubMed]
17. Grace, R.F.; Zanella, A.; Neufeld, E.J.; Morton, D.H.; Eber, S.; Yaish, H.; Glader, B. Erythrocyte pyruvate kinase deficiency: 2015 status report. *Am. J. Hematol.* **2015**, *90*, 825–830. [CrossRef] [PubMed]
18. Koralkova, P.; van Solinge, W.W.; van Wijk, R. Rare hereditary red blood cell enzymopathies associated with hemolytic anemia—Pathophysiology, clinical aspects, and laboratory diagnosis. *Int. J. Lab. Hematol.* **2014**, *36*, 388–397. [CrossRef] [PubMed]

19. Grace, R.F.; Bianchi, P.; van Beers, E.J.; Eber, S.W.; Glader, B.; Yaish, H.M.; Despotovic, J.M.; Rothman, J.A.; Sharma, M.; McNaull, M.M.; et al. Clinical spectrum of pyruvate kinase deficiency: Data from the Pyruvate Kinase Deficiency Natural History Study. *Blood* **2018**, *131*, 2183–2192. [CrossRef]

20. Kung, C.; Hixon, J.; Kosinski, P.A.; Cianchetta, G.; Histen, G.; Chen, Y.; Hill, C.; Gross, S.; Si, Y.; Johnson, K.; et al. AG-348 enhances pyruvate kinase activity in red blood cells from patients with pyruvate kinase deficiency. *Blood* **2017**, *130*, 1347–1356. [CrossRef]

21. Rab, M.A.E.; Van Oirschot, B.A.; Kosinski, P.A.; Hixon, J.; Johnson, K.; Chubukov, V.; Dang, L.; Pasterkamp, G.; Van Straaten, S.; Van Solinge, W.W.; et al. AG-348 (Mitapivat), an allosteric activator of red blood cell pyruvate kinase, increases enzymatic activity, protein stability, and ATP levels over a broad range of PKLR genotypes. *Haematologica* **2021**, *106*, 238–249. [CrossRef] [PubMed]

22. Li, C.; Wen, A.; Shen, B.; Lu, J.; Huang, Y.; Chang, Y. FastCloning: A highly simplified, purification-free, sequence- and ligation-independent PCR cloning method. *BMC Biotechnol.* **2011**, *11*, 92. [CrossRef] [PubMed]

23. Vonrhein, C.; Flensburg, C.; Keller, P.; Sharff, A.; Smart, O.; Paciorek, W.; Womack, T.; Bricogne, G. Data processing and analysis with the autoPROC toolbox. *Acta Crystallogr. Sect. D Struct. Biol.* **2011**, *67*, 293–302. [CrossRef] [PubMed]

24. McCoy, A.J.; Grosse-Kunstleve, R.W.; Adams, P.D.; Winn, M.D.; Storoni, L.C.; Read, R.J. Phaser crystallographic software. *J. Appl. Crystallogr.* **2007**, *40*, 658–674. [CrossRef] [PubMed]

25. Emsley, P.; Lohkamp, B.; Scott, W.G.; Cowtan, K. Features and development of Coot. *Acta Crystallogr. Sect. D Biol. Crystallogr.* **2010**, *66*, 486–501. [CrossRef] [PubMed]

26. Afonine, P.V.; Grosse-Kunstleve, R.W.; Echols, N.; Headd, J.J.; Moriarty, N.W.; Mustyakimov, M.; Terwilliger, T.C.; Urzhumtsev, A.; Zwart, P.H.; Adams, P.D. Towards automated crystallographic structure refinement with phenix.refine. *Acta Crystallogr. Sect. D Biol. Crystallogr.* **2012**, *68*, 352–367. [CrossRef] [PubMed]

27. Berkholz, D.S.; Shapovalov, M.V.; Dunbrack, R.L., Jr.; Karplus, P.A. Conformation dependence of backbone geometry in proteins. *Structure* **2009**, *17*, 1316–1325. [CrossRef] [PubMed]

28. Williams, C.J.; Headd, J.J.; Moriarty, N.W.; Prisant, M.G.; Videau, L.L.; Deis, L.N.; Verma, V.; Keedy, D.A.; Hintze, B.J.; Chen, V.B.; et al. MolProbity: More and better reference data for improved all-atom structure validation. *Protein Sci.* **2018**, *27*, 293–315. [CrossRef]

29. Diedrich, K.; Krause, B.; Berg, O.; Rarey, M. PoseEdit: Enhanced ligand binding mode communication by interactive 2D diagrams. *J. Comput. Mol. Des.* **2023**, *37*, 491–503. [CrossRef]

30. Brautigam, C.A.; Zhao, H.; Vargas, C.; Keller, S.; Schuck, P. Integration and global analysis of isothermal titration calorimetry data for studying macromolecular interactions. *Nat. Protoc.* **2016**, *11*, 882–894. [CrossRef]

31. Nain-Perez, A.; Nilsson, O.; Lulla, A.; Haversen, L.; Brear, P.; Liljenberg, S.; Hyvonen, M.; Boren, J.; Grotli, M. Tuning liver pyruvate kinase activity up or down with a new class of allosteric modulators. *Eur. J. Med. Chem.* **2023**, *250*, 115177. [CrossRef] [PubMed]